International Journal of Automation and Computing 16(5), October 2019, 604-613
DOI: 10.1007/s11633-018-1157-4

Predictive Adaptive Kalman Filter and Its Application to INS/UWB-integrated Human Localization with Missing UWB-based Measurements

Yuan Xu[1] Tao Shen[1] Xi-Yuan Chen[2] Li-Li Bu[1] Ning Feng[1]

[1] School of Electrical Engineering, University of Jinan, Jinan 250022, China

[2] School of Instrument Science and Engineering, Southeast University, Nanjing 210096, China

Abstract: In order to improve the accuracy of the data fusion filter, a tightly-coupled ultra wide band (UWB)/inertial navigation system (INS)-integrated scheme for indoor human navigation will be investigated in this paper. In this scheme, the data fusion filter employs the difference between the INS-measured and UWB-measured distances as the observation. Moreover, the predictive adaptive Kalman filter (PAKF) for the tightly-coupled INS/UWB-integrated human tracking model with missing data of the UWB-measured distance will be designed, which considers the missing data of the UWB-based distance and employs the predictive UWB-measured distance. Real test results will be done to compare the performance of the Kalman filter (KF), adaptive Kalman filter (AKF), and the PAKF. The test results show that the performance of the AKF is better than the KF. Moreover, the proposed PAKF is able to maintain the performance of the filter when the UWB-based measurement is unavailable.

Keywords: Indoor human localization, tightly-coupled model, predictive filtering, Kalman filter, missing data.

1 Introduction

In recent years, the topic on the human localization has received great attention[1, 2], which will satisfy the increased demand of the pedestrian navigation. Consequently, many approaches have been proposed[3–7]. The proposed approaches include two aspects: 1) the localization technology, 2) accurate data fusion filter.

In localization technology, global navigation satellite systems (GNSS)[8] have been widely used, and one famous example is the global positioning systems (GPS)[9]. There are many examples based on GPS, e.g., the dynamic target GPS localization algorithm has been designed[10]. A robust single GPS navigation and positioning algorithm has been proposed[11]. It should be emphasized that although the GNSS can provide accurate navigation information in outdoor environments, its performance is poor in indoor environments since its signal is easily impaired in indoor environments due to the obstructions from buildings. In order to compensate for the outage of GNSS, location based service (LBS)-based approaches have been designed[3, 12–14]. Many short-range communication technologies have been employed for this topic, such as radio frequency identification (RFID)[15], WiFi[16], and ultra wide band (UWB)[17]. RFID has been used to provide the human position information[18], meanwhile, an indoor localization algorithm with passive RFID tags is designed[18]. The WiFi has been used for indoor localization[19]. It should be pointed out that accuracy of the RFID-based and WiFi-based method is meter-level, which is not suitable for the high precision indoor navigation and positioning. In order to improve the accuracy of the location precision, the ultra wide band (UWB) is employed for the indoor environment. For instance, a fast 3D localization in multipath for UWB wireless sensor networks is proposed[20]. Meanwhile, a UWB-based indoor human localization system has been proposed[4]. It should be pointed out that the LBS-based approaches mentioned above depend on the prearranged reference nodes (RNs), however, the RNs are not easily arranged in some places. In order to overcome this problem, the self-contained method has been proposed, which employs the inertial measurement unit (IMU) to provide the navigation information of the target human alone. And the inertial navigation system (INS) is one of the most widely used examples. For instance, robust self-contained pedestrian navigation by fusing the IMU and compass measurements has been designed for indoor environment[21]. Pedestrian tracking with shoe-mounted IMU has been proposed[22]. It should be pointed out that the INS is not good at long-term working due to error accumulation.

Research Article
Manuscript received May 30, 2018; accepted August 23, 2018; published online November 6, 2018
Recommended by Associate Editor Yi Cao

In order to overcome the GNSS-based, the LBS-based, and the INS-based shortcomings, the integrated localization scheme has been used[23–25]. One can find many approaches to the topic of integrated navigation for the outdoor and indoor environment. For instance, in order to obtain higher precision navigation information, INS/GNSS-integrated system has been proposed[9, 26], a GPS/(BeiDou navigation satellite system) BDS/INS tightly-coupled integration has been used[27]. For the indoor environment, the INS/UWB-integrated system for the indoor human localization has been proposed[28]. Meanwhile, the handheld devices-based pedestrian dead reckoning (PDR)/INS/WiFi-integrated system has been used for indoor pedestrian navigation[29]. It should be pointed out that although the integrated localization scheme is able to overcome the shortcomings of the single localization technology, the outage of the single localization technology may prevent the integrated navigation system from working.

On the other hand, the performance of integrated navigation also depends on performance of the data fusion filter. And the Kalman filter (KF) is widely used in the field of the data fusion for the integrated navigation[30–34], which demonstrates definitive improvements on the optimal estimation. For example, the KF is used to correct the error drift of the INS[35, 36]. And the KF is designed for pedestrian localization[37]. It should be pointed out that the KF-based filters have to utilize the accurate noise statistics to obtain good performance[38–41]. Moreover, in the field of the data fusion filter for the pedestrian tracking, the missing data is not considered in the approaches mentioned above.

In this paper, in order to improve the accuracy of the data fusion filter, a tightly-coupled UWB/INS-integrated scheme for indoor human navigation will be investigated. In this scheme, the data fusion filter employs the difference between the INS-measured and UWB-measured distances as the observation. Moreover, the predictive adaptive Kalman filter (PAKF) for the tightly-coupled INS/UWB-integrated human tracking model with missing data of the UWB-measured distance will be designed, which considers the missing data of the UWB-based distance and employs the predictive UWB-measured distance. The main contribution of this work is to design a KF-based filter to fuse the INS-derived and UWB-derived measurements with missing data. Real test results will be done to compare the performance of the Kalman filter (KF), adaptive Kalman filter (AKF), and the PAKF. The test results show that the performance of the AKF is better than the KF. Moreover, the proposed PAKF is able to maintain the performance of the filter when the UWB-based measurement is unavailable.

The work is organized as follows. The tightly-coupled INS/UWB-integrated pedestrian tracking scheme with missing UWB-dated data will be discussed in Section 2. Then, the predictive adaptive KF will be designed in Section 3. The real indoor tests of human localization using the proposed predictive adaptive KF are discussed in Section 4. Finally, conclusions are given in Section 5.

2 Tightly-coupled INS/UWB-integrated pedestrian localization scheme

In this section, the tightly-coupled INS/UWB-integrated scheme and the system model used in this paper will be investigated.

2.1 Tightly-coupled INS/UWB-integrated scheme

The tightly-coupled INS/UWB-integrated scheme is shown in Fig. 1. In this scheme, the UWB-measured distance $d_i^U, i \in (1, g)$ and the INS-measured distance $d_i^I, i \in (1, g)$ are computing simultaneously. Here, i is the ID of the reference node (RN), and g is the number of the RN. In this paper, only the projection distances are considered. The difference of d_i^U and d_i^I is used by the PAKF to estimate the INS position error, which is used to correct the INS position.

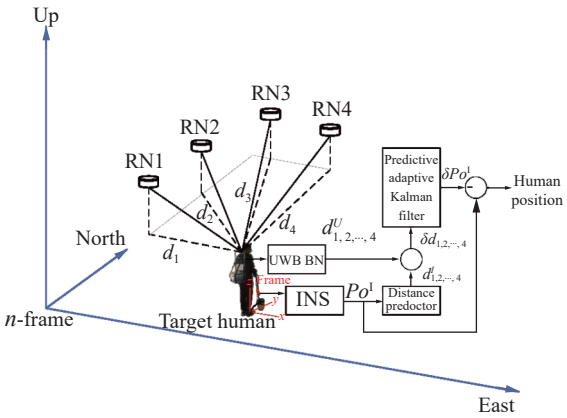

Fig. 1 Block diagram of the tightly-coupled INS/UWB-integrated scheme

2.2 System model

In this subsection, the state and the measurement equations are designed. In this paper, an INS error model with 15-elements is used, which we have used in [42, 43]. The state equation used in this work is listed in (1). Where the attitude, velocity, and position errors vector of INS at time index t are denoted as ϕ_t, $\delta \boldsymbol{V}_t^n$, and $\delta \boldsymbol{P}_t^n$ respectively, $\left(\nabla_t^b, \varepsilon_t^b\right)$ are the vectors of the accelerometer's bias and gyroscope drift at time index t, T is the sampling time, $\omega_t \sim N(0, \boldsymbol{Q})$ is the system noise. $\boldsymbol{C}_b^n$ and $S\left(\boldsymbol{f}_k^n\right)$ can be computed by (2).

$$\underbrace{\begin{bmatrix}\phi_t\\ \delta\boldsymbol{V}_t^n\\ \delta\boldsymbol{P}_t^n\\ \nabla_t^b\\ \varepsilon_t^b\end{bmatrix}}_{\boldsymbol{X}_{t|t-1}}=\underbrace{\begin{bmatrix}\boldsymbol{I}_{3\times3} & \boldsymbol{0}_{3\times3} & \boldsymbol{0}_{3\times3} & \boldsymbol{0}_{3\times3} & -\boldsymbol{I}_{3\times3}\boldsymbol{C}_b^nT\\ S\left(\boldsymbol{f}_t^n\right)T & \boldsymbol{I}_{3\times3} & \boldsymbol{0}_{3\times3} & \boldsymbol{I}_{3\times3}\boldsymbol{C}_b^nT & \boldsymbol{0}_{3\times3}\\ \boldsymbol{0}_{3\times3} & \boldsymbol{I}_{3\times3}T & \boldsymbol{I}_{3\times3} & \boldsymbol{0}_{3\times3} & \boldsymbol{0}_{3\times3}\\ \boldsymbol{0}_{3\times3} & \boldsymbol{0}_{3\times3} & \boldsymbol{0}_{3\times3} & \boldsymbol{I}_{3\times3} & \boldsymbol{0}_{3\times3}\\ \boldsymbol{0}_{3\times3} & \boldsymbol{0}_{3\times3} & \boldsymbol{0}_{3\times3} & \boldsymbol{0}_{3\times3} & \boldsymbol{I}_{3\times3}\end{bmatrix}}_{\boldsymbol{F}_t}\underbrace{\begin{bmatrix}\phi_{t-1}\\ \delta\boldsymbol{V}_{t-1}^n\\ \delta\boldsymbol{P}_{t-1}^n\\ \nabla_{t-1}^b\\ \varepsilon_{t-1}^b\end{bmatrix}}_{\boldsymbol{X}_{t-1}}+\boldsymbol{\omega}_{t-1}. \tag{1}$$

$$\boldsymbol{C}_b^n=\begin{bmatrix}\cos\gamma & 0 & -\sin\gamma\\ 0 & 1 & 0\\ \sin\gamma & 0 & \cos\gamma\end{bmatrix}\begin{bmatrix}1 & 0 & 0\\ 0 & \cos\theta & \sin\theta\\ 0 & -\sin\theta & \cos\theta\end{bmatrix}\begin{bmatrix}\cos\psi & -\sin\psi & 0\\ \sin\psi & \cos\psi & 0\\ 0 & 0 & 1\end{bmatrix},\ S\left(\boldsymbol{f}_t^n\right)=\begin{bmatrix}0 & f_{Ut}^n & -f_{Nt}^n\\ -f_{Ut}^n & 0 & f_{Et}^n\\ f_{Nt}^n & -f_{Et}^n & 0\end{bmatrix}. \tag{2}$$

It should be emphasized that the i-th UWB-derived distance is easily unavailable in indoor environments, which will affect the positioning accuracy of integrated scheme. In this paper, the variable $\alpha_t^i, i\in(1,2,\cdots,g)$ is employed to indicate the UWB-derived missing data.

When $\alpha_t^i=1$, it means that the UWB-derived distance is available. The INS-measured distance between the RN and the target person at time index t can be written as follows:

$$d_{i,t}^I=\sqrt{\left(P_{E,t}^I-P_E^{(i)}\right)+\left(P_{N,t}^I-P_N^{(i)}\right)},\ i=1,2,\cdots,g \tag{3}$$

where $P_{E,t}^I$ and $P_{N,t}^I$ denote the INS positions in east and north directions at time index t, $P_E^{(i)}$ and $P_N^{(i)}$ denote the positions of the i-th RN in east and north direction.

Here, (3) can be rewritten by the first-order Taylor expansion at real position of the target person $(P_{E,t},P_{N,t})$:

$$d_{i,t}^I=\underbrace{\sqrt{\left(P_{E,t}-P_E^{(i)}\right)+\left(P_{N,t}-P_N^{(i)}\right)}}_{d_{i,t}}+\frac{\partial d_{i,t}^I}{\partial P_{E,t}}\delta P_{E,t}+\frac{\partial d_{i,t}^I}{\partial P_{N,t}}\delta P_{N,t},\ i=1,2,\cdots,g \tag{4}$$

where $(\delta P_{E,t},\delta P_{N,t})$ is the INS position error in n-frame at time index t. To the UWB-based distance, we can get the following expression:

$$d_{i,t}^U=d_{i,t}+\boldsymbol{v}_{i,t},\ i=1,2,\cdots,g. \tag{5}$$

Thus, we can obtain:

$$\delta d_{i,t}=d_{i,t}^I-d_{i,t}^U=\frac{\partial d_{i,t}^I}{\partial P_{E,t}}\delta P_{E,t}+\frac{\partial d_{i,t}^I}{\partial P_{N,t}}\delta P_{N,t},\ i=1,2,\cdots,g. \tag{6}$$

Then, the measurement equation when $\alpha_t=1$ can be written as

$$\underbrace{\begin{bmatrix}\delta d_{1,t}\\ \delta d_{2,t}\\ \vdots\\ \delta d_{g,t}\end{bmatrix}_{g\times1}}_{\boldsymbol{Y}_t}=\begin{bmatrix}d_{1,t}^I-d_{1,t}^U\\ d_{2,t}^I-d_{2,t}^U\\ \vdots\\ d_{g,t}^I-d_{g,t}^U\end{bmatrix}_{g\times1}=\boldsymbol{H}_t\boldsymbol{X}_t+\nu_t \tag{7}$$

where $\nu_t\sim N(0,\boldsymbol{R}_t)$ is the measurement noise, and

$$\boldsymbol{H}_t=\begin{bmatrix}\boldsymbol{0}_{3\times3} & \boldsymbol{0}_{3\times3} & \frac{\partial d_{1,t}^I}{\partial P_{E,t}} & \frac{\partial d_{1,t}^I}{\partial P_{N,t}} & 0 & \boldsymbol{0}_{3\times3} & \boldsymbol{0}_{3\times3}\\ \boldsymbol{0}_{3\times3} & \boldsymbol{0}_{3\times3} & \frac{\partial d_{2,t}^I}{\partial P_{E,t}} & \frac{\partial d_{2,t}^I}{\partial P_{N,t}} & 0 & \boldsymbol{0}_{3\times3} & \boldsymbol{0}_{3\times3}\\ \vdots & \vdots & \vdots & \vdots & \vdots & \vdots & \vdots\\ \boldsymbol{0}_{3\times3} & \boldsymbol{0}_{3\times3} & \frac{\partial d_{g,t}^I}{\partial P_{E,t}} & \frac{\partial d_{g,t}^I}{\partial P_{N,t}} & 0 & \boldsymbol{0}_{3\times3} & \boldsymbol{0}_{3\times3}\end{bmatrix}_{g\times15}. \tag{8}$$

The detailed derivation of the measurement equation can be found in [42]. Once the i-th UWB-based distance is unavailable, $\alpha_t^i=0$, and the observation for the data fusion filter can be predicted by

$$\underbrace{\begin{bmatrix}\delta d_{1,t}\\ \delta d_{i,t}\\ \vdots\\ \delta d_{g,t}\end{bmatrix}_{g\times1}}_{\tilde{\boldsymbol{Y}}_t}=\begin{bmatrix}d_{1,t}^I-d_{1,t}^U\\ \boldsymbol{H}_tF_{t-1}\boldsymbol{X}_{t-1}(i,1)\\ \vdots\\ d_{g,t}^I-d_{g,t}^U\end{bmatrix}_{g\times1},\ i\in(1,2,\cdots,g) \tag{9}$$

where $\delta d_{i,t}, i\in(1,2,\cdots,g)$ denotes the unavailable UWB-based distance. $\boldsymbol{H}_tF_{t-1}\boldsymbol{X}_{t-1}(i,1)$ denotes the i-th row and the 1st column of the $\boldsymbol{H}_tF_{t-1}\boldsymbol{X}_{t-1}(i,1)$. Thus, the system with missing data can be represented by

$$\begin{cases}\boldsymbol{X}_{t|t-1}=\boldsymbol{F}_{t-1}\boldsymbol{X}_{t-1}+\omega_{t-1}\\ \tilde{\boldsymbol{Y}}_{\alpha_t^i,t}=\begin{bmatrix}d_{1,t}^I-d_{1,t}^U\\ \boldsymbol{H}_tF_{t-1}\boldsymbol{X}_{t-1}(i,1)\\ \vdots\\ d_{g,t}^I-d_{g,t}^U\end{bmatrix}_{g\times1}\\ \boldsymbol{Y}_t=\alpha_t^i\left(\boldsymbol{H}_t\boldsymbol{X}_{t|t-1}+\nu_t\right)+\left(1-\alpha_t^i\right)\tilde{\boldsymbol{Y}}_{\alpha_t^i,t}.\end{cases} \tag{10}$$

3 Filters for indoor pedestrian tracking

In this section, the adaptive KF (AKF) and the improving predictive AKF (PAKF) for the system proposed in Section 2.2 will be designed.

3.1 Adaptive Kalman filter

For the data fusion filter, the KF has been widely used, however, it should be pointed out that the perform-

ance of the KF depends on the model and the noise statistics. When the data fusion model is designed, it is hard for the fixed noise description to satisfy its actual application. In order to overcome this problem, the AKF has been proposed, which employs the dynamic noise description. The pseudo code of the AKF for the systems (1) and (3) is sketched in Algorithm 1. Compared with the basic Kalman filter, the adaptive Kalman filter computes the $\boldsymbol{R}_t$ at each time index (line 8–11).

Algorithm 1. Adaptive Kalman filter

1) **Data:** $\boldsymbol{Y}_t$, $\boldsymbol{X}_0$, $\boldsymbol{P}_0$, $\boldsymbol{Q}$, $\boldsymbol{R}_0$
2) **Result:** $\hat{\boldsymbol{X}}_t$
3) **begin**
4) **for** $t = 1 : \infty$ **do**
5) $\hat{\boldsymbol{X}}_{t|t-1} = \boldsymbol{F}_t \hat{\boldsymbol{X}}_{t-1}$
6) $\boldsymbol{P}_{t|t-1} = \boldsymbol{F}_{t-1} \boldsymbol{P}_{t-1} \boldsymbol{F}_{t-1}^{\mathrm{T}} + \boldsymbol{Q}$
7) $\boldsymbol{K}_t = \boldsymbol{P}_{t|t-1} \boldsymbol{H}_t^{\mathrm{T}} \left(\boldsymbol{H}_t \boldsymbol{P}_{t|t-1} \boldsymbol{H}_t^{\mathrm{T}} + \boldsymbol{R}_t \right)^{-1}$
8) $\hat{\boldsymbol{X}}_t = \hat{\boldsymbol{X}}_{t|t-1} + \boldsymbol{K}_t (\boldsymbol{Y}_t - \boldsymbol{H}_t \hat{\boldsymbol{X}}_{t|t-1})$
9) $\boldsymbol{P}_t = (\boldsymbol{I} - \boldsymbol{K}_t \boldsymbol{H}_t) \boldsymbol{P}_{t|t-1}$
10) $\boldsymbol{v}_t = \boldsymbol{Y}_t - \boldsymbol{H}_t \hat{\boldsymbol{X}}_{t|t-1} - \boldsymbol{r}_t$
11) $\boldsymbol{r}_t = (1 - d_t)\, \boldsymbol{r}_{t-1} + d_{t-1} (\boldsymbol{Y}_t - \boldsymbol{H}_t \hat{\boldsymbol{X}}_{t|t-1})$
12) $\boldsymbol{R}_t = (1 - d_{t-1})\, \boldsymbol{R}_{t-1} + d_{t-1} \left(\boldsymbol{v}_t \boldsymbol{v}_t^{\mathrm{T}} - \boldsymbol{H}_t \boldsymbol{P}_{t|t-1} \boldsymbol{H}_t^{\mathrm{T}} \right)$
13) $d_{t-1} = \dfrac{1-b}{1-b^t}, 0 < b < 1$
14) **end for**
15) **end**

3.2 Predictive adaptive Kalman filter

For the system (10), the pseudo code of the improving predictive adaptive Kalman filter is sketched in Algorithm 2. In the improving predictive AKF algorithm, the outage of the UWB-based data is considered (line 6–8). The variable α_t is employed to indicate the UWB-derived missing data, and the predictive UWB-based distance is used as the observation for the filter when the UWB is outage.

Algorithm 2. Predictive adaptive Kalman filter

1) **Data:** $\boldsymbol{Y}_t$, $\boldsymbol{X}_0$, $\boldsymbol{P}_0$, $\boldsymbol{Q}$, $\boldsymbol{R}_0$
2) **Result:** $\hat{\boldsymbol{X}}_t$
3) **begin**
4) **for** $t = 1 : \infty$ **do**
5) $\hat{\boldsymbol{X}}_{t|t-1} = \boldsymbol{F}_t \hat{\boldsymbol{X}}_{t-1}$
6) $\boldsymbol{P}_{t|t-1} = \boldsymbol{F}_{t-1} \boldsymbol{P}_{t-1} \boldsymbol{F}_{t-1}^{\mathrm{T}} + \boldsymbol{Q}$
7) **if** $\alpha_t^i = 0$ **then**
8) $\boldsymbol{Y}_t = \begin{bmatrix} d_{1,t}^I - d_{1,t}^U \\ \boldsymbol{H}_t F_{t-1} \boldsymbol{X}_{t-1}(i,1) \\ \vdots \\ d_{g,t}^I - d_{g,t}^U \end{bmatrix}_{g \times 1}$
9) **end if**
10) $\boldsymbol{K}_t = \boldsymbol{P}_{t|t-1} \boldsymbol{H}_t^{\mathrm{T}} \left(\boldsymbol{H}_t \boldsymbol{P}_{t|t-1} \boldsymbol{H}_t^{\mathrm{T}} + \boldsymbol{R}_t \right)^{-1}$
11) $\hat{\boldsymbol{X}}_t = \hat{\boldsymbol{X}}_{t|t-1} + \boldsymbol{K}_t (\boldsymbol{Y}_t - \boldsymbol{H}_t \hat{\boldsymbol{X}}_{t|t-1})$
12) $\boldsymbol{P}_t = (\boldsymbol{I} - \boldsymbol{K}_t \boldsymbol{H}_t) \boldsymbol{P}_{t|t-1}$
13) $\boldsymbol{v}_t = \boldsymbol{Y}_t - \boldsymbol{H}_t \hat{\boldsymbol{X}}_{t|t-1} - \boldsymbol{r}_t$
14) $\boldsymbol{r}_t = (1 - d_t)\, \boldsymbol{r}_{t-1} + d_{t-1} (\boldsymbol{Y}_t - \boldsymbol{H}_t \hat{\boldsymbol{X}}_{t|t-1})$
15) $\boldsymbol{R}_t = (1 - d_{t-1})\, \boldsymbol{R}_{t-1} + d_{t-1} \left(\boldsymbol{v}_t \boldsymbol{v}_t^{\mathrm{T}} - \boldsymbol{H}_t \boldsymbol{P}_{t|t-1} \boldsymbol{H}_t^{\mathrm{T}} \right)$
16) $d_{t-1} = \dfrac{(1-b)}{(1-b^t)}, 0 < b < 1$
17) **end for**
18) **end**

4 Real indoor test

In this section, the real test for the verification of the performance of the improving PAKF proposed in the paper will be investigated, which has been done in the Machine Building of the University of Jinan, China. Firstly, the test environment and the setting will be designed. Secondly, the performance of the KF and AKF will be compared. Finally, the outage of the UWB will be simulated and the performance of the AKF and the PAKF will be investigated.

4.1 Test environment

Figs. 2 and 3 sketch the test environment and the equipment used by the target human in the test. Moreover, Fig. 4 displays the structure of the experimental platform used in the test. The UWB localization system used in the test includes the 4 UWB RNs and the UWB BN. Here, the UWB RNs are fixed on the known coordinates. And the UWB BN is fixed on the target human. In this test, the UWB localization system to provide the UWB-based distance $d_i^U, i \in (1, g)$ between the UWB RN and the target human. Meanwhile, the foot-mounted inertial measurement unit (IMU) is used to provide the INS-based position, which is used to compute the INS-based distance $d_i^I, i \in (1, g)$ between the UWB RN and the target human. As shown in Figs. 1 and 4, it should be emphasized that we employ the projection distances since only the 2D localization is considered. Moreover, in order to provide the reference value, we employ the following steps:

1) Build the mapping between the distance l_t from the start point and the reference position at time index t.

Fig. 2 The test environment

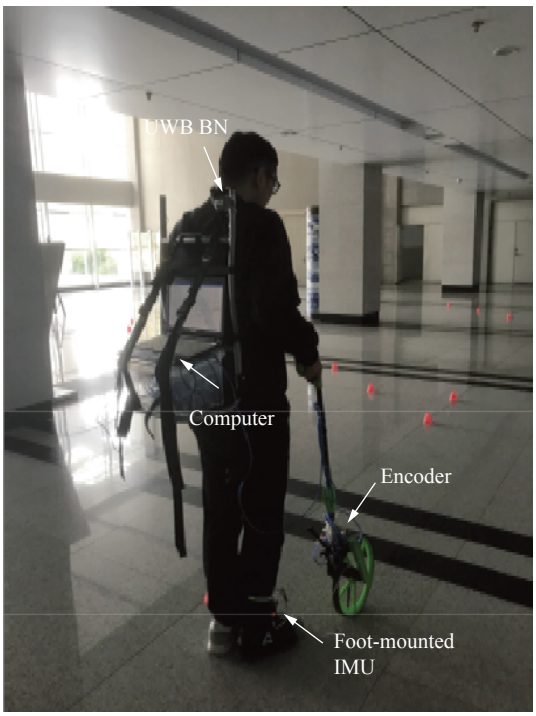

Fig. 3 Target person with the equipment used in the test

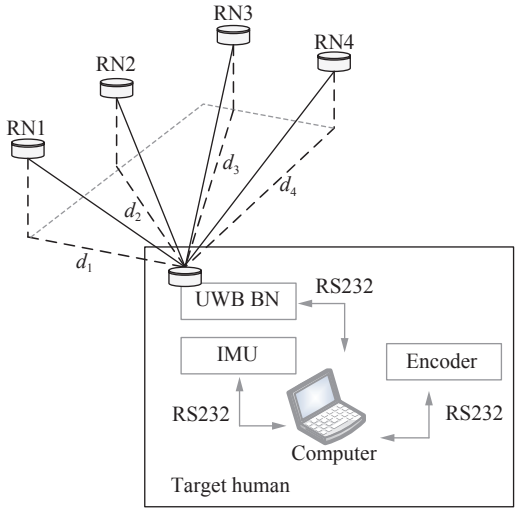

Fig. 4 Structure of the experimental platform used in the test

2) Measure l_t via the encoder.

3) The reference position value at time index t can be computed via the encoder measured by the encode and the mapping built in the first step.

For the filter, in this paper, we set $T = 0.1$ s, $\boldsymbol{Q} = 10^{-1} \times \boldsymbol{I}_{15\times15}$, $\boldsymbol{R}_0 = 10^{-1} \times \boldsymbol{I}_{4\times15}$, $b = 0.95$.

4.2 Performance comparison between INS and UWB

In the real test, the target human walked from the start point to the end point following the planned reference path. In order to improve the accuracy of the INS position, the zero velocity update (ZUPT) is used by the INS (so-called INS+ZUPT). The principles of the ZUPT can be found in [35], which is to use the data fusion filter to correct the error drift of INS via the measurement when the feet fall on the ground. The planned reference path, the trajectories measured by the UWB and INS with ZUPT are shown in Fig. 5, which are denoted as black line, green line, and blue dashed respectively. Meanwhile, the positions of the UWB RNs are also marked in Fig. 5 (cross). From Fig. 5, it can be seen obviously that the path estimated by the INS appears the error accumulation. Although the ZUPT can reduce the INS position error effectively, it still has the challenge of long-term working. At the end of the test, the error of the INS position is big, which demonstrates that the INS solution is not good at long-term navigation. Compared with the INS solution, the position provided by the UWB is always close to the reference path. The size of the IMU used in the paper is $48 \times 28 \times 13$ mm ($length \times width \times height$), and it weighs 20 g, the performance of the IMU used in this paper are summarized in Table. 1.

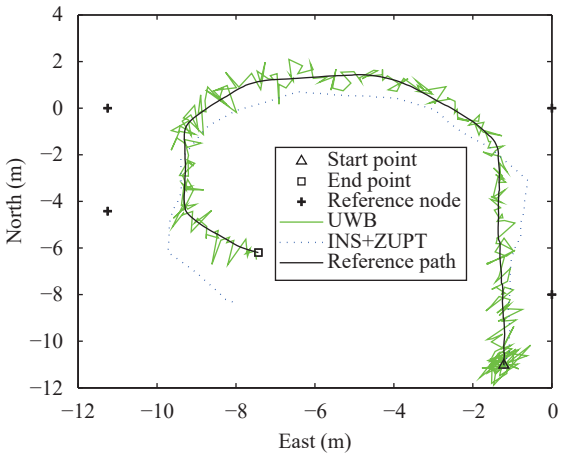

Fig. 5 The reference path (black line) and the trajectories measured from the INS with ZUPT (blue dashed) and UWB (green line). Color versions of the figures in this paper are available online.

Table 1 Performance of the IMU used in this paper

	Accelerometers	Gyroscopes	Magnetometers
Axes	3	3	3
Full scale	±5 g	±300 deg/s	±8 Gauss
Analog-to-digital converter (ADC) bit	16	16	12
Update rate	1–100 Hz	1–100 Hz	1–100 Hz

The INS-derived and UWB-derived east and north position errors are sketched in Figs. 6 and 7. In Figs. 6 and 7, the INS position error is depicted with blue line, and the UWB position error is depicted with green line. From Figs. 6 and 7, we can get a conclusion similar to that in

Fig. 5. The INS position errors are bigger than the UWB both in east and north directions, which demonstrates that the INS solution has error accumulation. Compared with the INS position error, the east position error of UWB is basically maintained between −0.5 m and 0.5 m, and the north position error of UWB is basically maintained between −1 m and 1 m. It can be seen easily that the UWB solution is stable, as it does not have the error drift. Moreover, Table 2 lists the mean-square errors (MSEs) of the position estimated by the INS and UWB. From Table 2, we can see that the MSEs of the position in east direction and north direction estimated by the UWB are 0.04 m and 0.11 m, which are smaller than that value of INS.

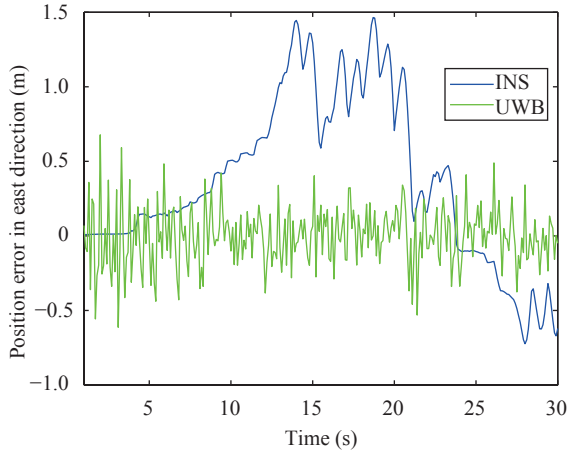

Fig. 6 The east position errors of the INS and UWB

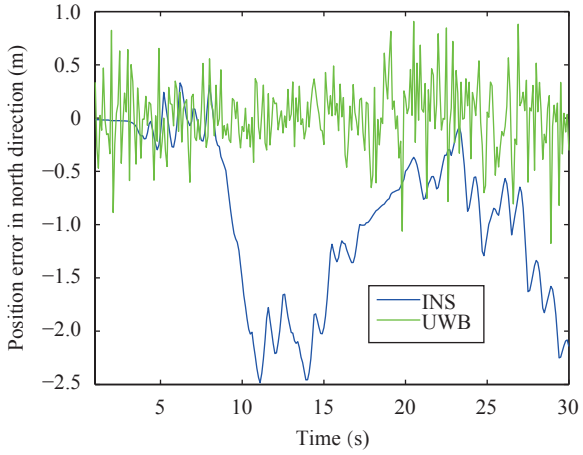

Fig. 7 The north position errors of the INS and UWB

Table 2 MSEs of the position estimated by the INS and UWB

Method	MSE (m^2)	
	East	North
INS	0.42	1.36
UWB	0.04	0.11

4.3 Performance comparison between KF and AKF

In this section, the performance of the KF and the AKF will be compared. Fig. 8 displays the trajectories measured from the KF and AKF. Here, the KF-derived path is depicted with a blue line, and the AKF-derived path is depicted with a red line. From Fig. 8, one can find that both the KF and the AKF are able to provide the path of the target human and reduce the position error effectively compared with the UWB solution (depicted with green line). Compared with the KF-derived trajectory, the performance of the AKF is better. One can see easily that the KF-derived trajectory has great errors in the final stage of the experiment. While the AKF-derived trajectory is always close to the reference trajectory.

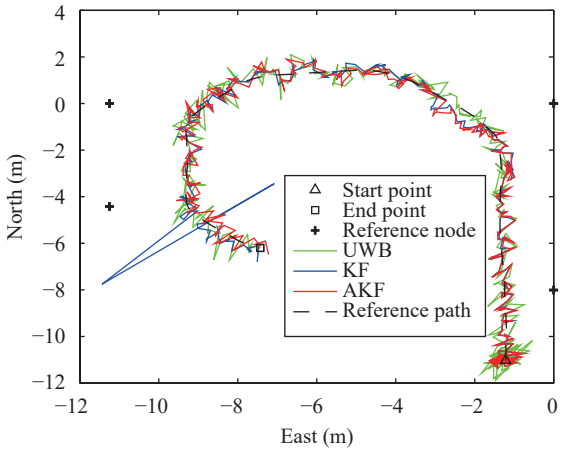

Fig. 8 The reference path (black line) and the trajectories measured from the UWB (green line), the KF (blue line) and AKF (red line)

In this subsection, the KF-derived and the AKF-derived solution are compared with the UWB solution only because the INS position error is bigger than the UWB solution, which has been discussed in Section 4.2. The east and north position errors derived by the KF and AKF are shown in Figs. 9 and 10. From Figs. 9 and 10, one can find that both the KF and AKF are effective in reducing the localization error for the target human. The position errors of the KF and the AKF are smaller than that value of the UWB in both the east and the north directions. At the end of the experiment, one can find that there is a big position error for KF, its value is even bigger than the UWB-solution. Compared with the KF-derived position error, the AKF-derived performance is stable. When there is a big position error for KF, the position error of the AKF is still lower than the UWB-derived position error. Table 3 lists the mean-square errors (MSEs) of the position estimated by the UWB, KF and AKF. From Table 3, we can see that the MSEs of the position in east and north directions estimated by the KF

are 0.06 m and 0.09 m respectively, which are bigger than that value of UWB due to the big position error at the end of the experiment. The MSE of the position in east and north directions estimated by the AKF are 0.03 m and 0.06 m respectively, which are the smallest.

4.4 Performance comparison between AKF and PAKF

In this section, the performance of the AKF and the PAKF will be compared. From Sections 2 and 3, it can be seen that the PAKF proposed in this paper is designed for the available UWB-measured distance. Thus, in this section, three outage areas are simulated (#1, #2 and #3), which is shown in Fig. 11 (depicted with red line). It should be emphasized that the simulated outage areas are different in this paper, as follows:

1) In the #1 simulated outage area, only one unavailable UWB-measured distance is simulated. Since this situation happens often, the size of this simulated outage area is 20 sample points.

2) In the #2 simulated outage area, two unavailable UWB-measured distances are simulated. The size of this simulated outage area is 15 sample points.

3) In the #3 simulated outage area, three unavailable UWB-measured distances are simulated. The size of this simulated outage area is 5 sample points since this situation does not happens often.

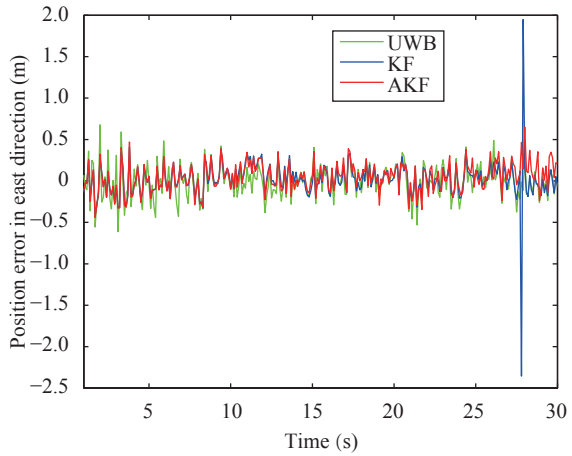

Fig. 9 East position errors of the UWB, KF and AKF

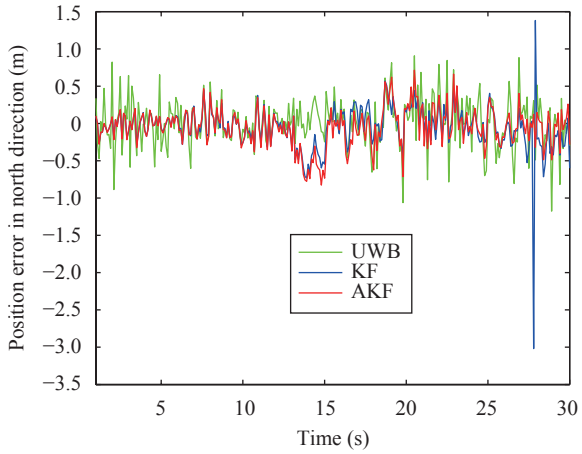

Fig. 10 North position errors of the UWB, KF and AKF

Table 3 MSEs of the position estimated by the UWB, KF and AKF

Method	MSE (m^2)	
	East	North
UWB	0.04	0.11
KF	0.06	0.09
AKF	0.03	0.06

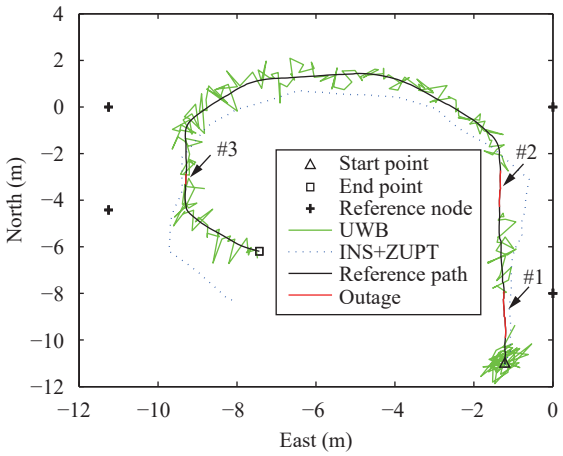

Fig. 11 The reference path (black line), the trajectories measured from the INS with ZUPT (blue dashed), the UWB (green line) and the missing data of UWBs (red line)

The east and north position errors derived by the UWB and the PAKF are shown in Figs. 12 and 13, respectively. Table 4 lists the MSEs of position measured by the INS, UWB, AKF and the PAKF. In Table 4, the "NaN" means "not a number", which indicates the value is unavailable. In Figs. 12 and 13 and Table 4, the UWB position error is depicted with a green line, the PAKF position error when the UWB-measured distance is available is depicted with a blue line, and the PAKF position error when the UWB-measured distance is unavailable is depicted with a blue line. From Figs. 12 and 13, we can see that there are three outages for the UWB, which the UWB-based measurement is unavailable. To the PAKF, it can be seen that the proposed method is able to work with the UWB-based missing measurement.

5 Conclusions

In this paper, a tightly-coupled INS/UWB-integrated scheme for the indoor human localization has been designed. In order to improve the accuracy of the data fu-

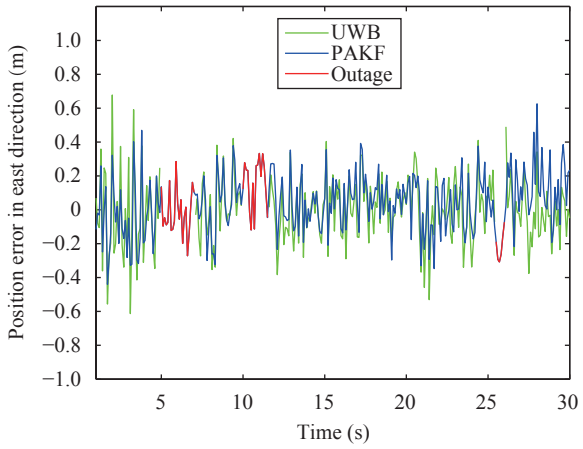

Fig. 12 East position errors of the UWB and PAKF

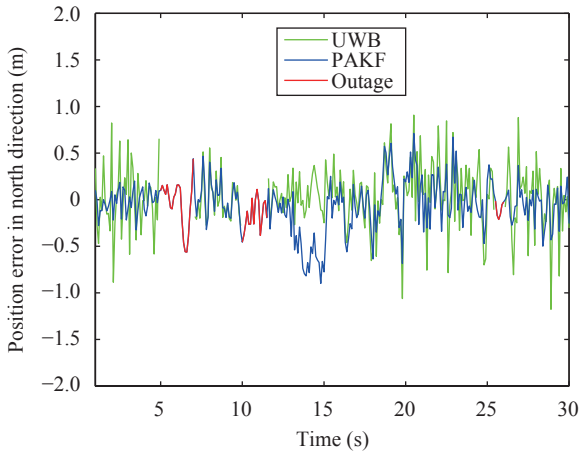

Fig. 13 North position errors of the UWB and PAKF

Table 4 MSEs of position measured by the INS, UWB, AKF and the PAKF

Model	MSE (m)	
	East	North
INS	0.42	1.36
UWB	NaN	NaN
AKF	NaN	NaN
PAKF	0.03	0.03

sion filter, the adaptive Kalman filter has been used as the main filter. Meanwhile, the outage of the UWB-measured distance has been considered. And the filter for the tightly-coupled INS/UWB-integrated human localization with missing measurement has been designed. The main contributions of this paper are listed as follows:

1) The INS-measured and UWB-measured distances have been employed as observations for the data fusion filter.

2) The PAKF has been proposed, which employs the predictive UWB-based distance to maintain the performance of the AKF.

The experimental results show that the performance of the AKF is better than the KF. Moreover, the proposed PAKF is able to maintain the performance of the filter when the UWB-based measurement is unavailable.

Acknowledgements

This work was supported by National Natural Science Foundation of China (Nos. 61803175 and 61773239), the China Postdoctoral Science Foundation (No. 2017 M622204), the Shandong Provincial Natural Science Foundation, China (Nos. ZR2018LF010 and ZR2015JL020), the High School Science and Technology Project in Shandong Province (No. J18KA333), and the Doctoral Foundation of the University of Jinan, China (No. XBS1503).

References

[1] A. R. J. Ruiz, F. S. Granja, J. C. P. Honorato, J. I. G. Rosas. Accurate pedestrian indoor navigation by tightly coupling foot-mounted IMU and RFID measurements. *IEEE Transactions on Instrumentation and Measurement*, vol. 61, no. 1, pp. 178–189, 2011. DOI: 10.1109/TIM.2011.2159317.

[2] M. Y. Zhang, G. H. Tian, C. C. Li, J. Gong. Learning to transform service instructions into actions with reinforcement learning and knowledge base. *International Journal of Automation and Computing*, vol. 15, no. 5, pp. 582–592, 2018. DOI: 10.1007/s11633-018-1128-9.

[3] J. Gimenez, A. Amicarelli, J. M. Toibero, F. Di Sciascio, R. Carelli. Iterated conditional modes to solve simultaneous localization and mapping in Markov random fields context. *International Journal of Automation and Computing*, vol. 15, no. 3, pp. 310–324, 2018. DOI: 10.1007/s11633-017-1109-4.

[4] Y. Xu, Y. S. Shmaliy, Y. Y. Li, X. Y. Chen. UWB-based indoor human localization with time-delayed data using EFIR filtering. *IEEE Access*, vol. 5, pp. 16676–16683, 2017. DOI: 10.1109/ACCESS.2017.2743213.

[5] Y. L. Sun, W. X. Meng, C. Li, N. Zhao, K. L. Zhao, N. T. Zhang. Human localization using multi-source heterogeneous data in indoor environments. *IEEE Access*, vol. 5, pp. 812–822, 2017. DOI: 10.1109/ACCESS.2017.2650953.

[6] Z. F. Wu, Q. Xu, Z. Y. Wang, B. Chen, Q. Xuan. Passive indoor human localization based on channel state information. *Journal of Harbin Engineering University*, vol. 38, no. 8, pp. 1328–1334, 2017. DOI: 10.11990/jheu.201605001. (in Chinese)

[7] C. L. Wang, T. M. Wang, J. H. Liang, Y. C. Zhang, Y. Zhou. Bearing-only visual SLAM for small unmanned aerial vehicles in GPS-denied environments. *International Journal of Automation and Computing*, vol. 10, no. 5, pp. 387–396, 2013. DOI: 10.1007/s11633-013-0735-8.

[8] J. Yang, J. F. Ma, X. N. Liu, L. N. Qi, Z. Wang, Y. Zhuang, L. X. Shi. A height constrained adaptive Kalman filtering based on climbing motion model for GNSS positioning. *IEEE Sensors Journal*, vol. 17, no. 21, pp. 7105–7113, 2017. DOI: 10.1109/JSEN.2017.2752751.

[9] Y. H. Liu, X. Q. Fan, C. Lv, J. Wu, L. Li, D. W. Ding. An innovative information fusion method with adaptive Kalman filter for integrated INS/GPS navigation of autonom-

ous vehicles. *Mechanical Systems and Signal Processing*, vol. 100, pp. 605–616, 2018. DOI: 10.1016/j.ymssp.2017.07.051.

[10] B. Y. Chen, Y. S. Sun, G. Y. Chen, Z. X. Sun, L. H.Wu. A dynamic target GPS localization algorithm based on Kalman filter. *Journal of Harbin University of Science and Technology*, vol. 21, no. 4, pp. 1–6, 2016. DOI: 10.15938/j.jhust.2016.04.001. (in Chinese)

[11] H. L. Xiong, J. Tang, H. J. Xu, W. S. Zhang, Z. F. Du. A robust single GPS navigation and positioning algorithm based on strong tracking filtering. *IEEE Sensors Journal*, vol. 18, no. 1, pp. 290–298, 2018. DOI: 10.1109/JSEN.2017.2767066.

[12] S. C. Zhou, R. Yan, J. X. Li, Y. K. Chen, H. J. Tang. A brain-inspired SLAM system based on ORB features. *International Journal of Automation and Computing*, vol. 14, no. 5, pp. 564–575, 2017. DOI: 10.1007/s11633-017-1090-y.

[13] X. H. Li, M. X. Miao, H. Liu, J. F. Ma, K. C. Li. An incentive mechanism for K-anonymity in LBS privacy protection based on credit mechanism. *Soft Computing*, vol. 21, no. 14, pp. 3907–3917, 2017. DOI: 10.1007/s00500-016-2040-2.

[14] A. M. Rao, K. Ramji, B. S. K. S. S. Rao, V. Vasu, C. Puneeth. Navigation of non-holonomic mobile robot using neuro-fuzzy logic with integrated safe boundary algorithm. *International Journal of Automation and Computing*, vol. 14, no. 3, pp. 285–294, 2017. DOI: 10.1007/s11633-016-1042-y.

[15] A. Sharma, A. T. Hoang, M. S. Reynolds. Long-range battery-free UHF RFID with a single wire transmission line. *IEEE Sensors Journal*, vol. 17, no. 17, pp. 5687–5693, 2017. DOI: 10.1109/JSEN.2017.2727494.

[16] Y. Zhuang, Y. Li, L. N. Qi, H. Y. Lan, J. Yang, N. El-Sheimy. A two-filter integration of MEMS sensors and WiFi fingerprinting for indoor positioning. *IEEE Sensors Journal*, vol. 16, no. 13, pp. 5125–5126, 2016. DOI: 10.1109/JSEN.2016.2567224.

[17] N. Decarli, F. Guidi, D. Dardari. Passive UWB RFID for tag localization: Architectures and design. *IEEE Sensors Journal*, vol. 16, no. 5, pp. 1385–1397, 2016. DOI: 10.1109/JSEN.2015.2497373.

[18] J. J. Pomarico-Franquiz, Y. S. Shmaliy. Accurate self-localization in RFID tag information grids using FIR filtering. *IEEE Transactions on Industrial Informatics*, vol. 10, no. 2, pp. 1317–1326, 2014. DOI: 10.1109/TII.2014.2310952.

[19] C. S. Wu, Z. Yang, Z. M. Zhou, Y. H. Liu, M. Y. Liu. Mitigating large errors in WiFi-based indoor localization for smartphones. *IEEE Transactions on Vehicular Technology*, vol. 66, no. 7, pp. 6246–6257, 2017. DOI: 10.1109/TVT.2016.2630713.

[20] H. Jiang, C. Liu, Y. Zhang, H. J. Cui. Fast 3D node localization in multipath for UWB wireless sensor networks using modified propagator method. *International Journal of Distributed Sensor Networks*, vol. 10, no. 2, 2014. DOI: 10.1155/2014/312535.

[21] M. Hou, Y. Xu, X. Liu. Robust self-contained pedestrian navigation by fusing the IMU and compass measurements via UFIR filtering. *Journal of Electrical and Computer Engineering*, vol. 2018, Article number 8401967, 2018. DOI: 10.1155/2018/8401967.

[22] E. Foxlin. Pedestrian tracking with shoe-mounted inertial sensors. *IEEE Computer Graphics and Applications*, vol. 25, no. 6, pp. 38–46, 2005. DOI: 10.1109/MCG.2005.140.

[23] M. Y. Zhong, J. Guo, Z. H. Yang. On real time performance evaluation of the inertial sensors for INS/GPS integrated systems. *IEEE Sensors Journal*, vol. 16, no. 17, pp. 6652–6661, 2016. DOI: 10.1109/JSEN.2016.2588140.

[24] X. M. Wang, W. B. Ni. An improved particle filter and its application to an INS/GPS integrated navigation system in a serious noisy scenario. *Measurement Science and Technology*, vol. 27, no. 9, Article number 095005, 2016. DOI: 10.1088/0957-0233/27/9/095005.

[25] G. C. Fan, D. Song, C. D. Xu. Modified observation model in tightly-coupled INS/GPS integration. *Journal of Beijing Institute of Technology*, vol. 26, no. 1, pp. 16–28, 2017. DOI: 10.15918/j.jbit1004-0579.201726.0104.

[26] M. Y. Zhong, J. Guo, D. H. Zhou. Adaptive in-flight alignment of INS/GPS systems for aerial mapping. *IEEE Transactions on Aerospace and Electronic Systems*, vol. 54, no. 3, pp. 1184–1196, 2018. DOI: 10.1109/TAES.2017.2776058.

[27] H. Z. Han, J. Wang. Robust GPS/BDS/INS tightly coupled integration with atmospheric constraints for long-range kinematic positioning. *GPS Solutions*, vol. 21, no. 3, pp. 1285–1299, 2017. DOI: 10.1007/s10291-017-0612-y.

[28] L. L. Bu, Y. Zhang, Y. Xu. Indoor pedestrian tracking by combining recent INS and UWB measurements. In *Proceedings of International Conference on Advanced Mechatronic Systems*, IEEE, Xiamen, China, pp. 244–248, 2017. DOI: 10.1109/ICAMechS.2017.8316479.

[29] Y. Zhuang, H. Y. Lan, Y. Li, N. El-Sheimy. PDR/INS/WiFi integration based on handheld devices for indoor pedestrian navigation. *Micromachines*, vol. 6, no. 6, pp. 793–812, 2015. DOI: 10.3390/mi6060793.

[30] T. Z. Lv, C. X. Zhao, H. F. Zhang. An improved fastSLAM algorithm based on revised genetic resampling and SR-UPF. *International Journal of Automation and Computing*, vol. 15, no. 3, pp. 325–334, 2018. DOI: 10.1007/s11633-016-1050-y.

[31] D. Nada, M. Bousbia-Salah, M. Bettayeb. Multi-sensor data fusion for wheelchair position estimation with unscented Kalman filter. *International Journal of Automation and Computing*, vol. 15, no. 2, pp. 207–217, 2018. DOI: 10.1007/s11633-017-1065-z.

[32] M. Zorzi. Robust Kalman filtering under model perturbations. *IEEE Transactions on Automatic Control*, vol. 62, no. 6, pp. 2902–2907, 2017. DOI: 10.1109/TAC.2016.2601879.

[33] J. Liu, B. G. Cai, J. Wang. Cooperative localization of connected vehicles: Integrating GNSS with DSRC using a robust cubature Kalman filter. *IEEE Transactions on Intelligent Transportation Systems*, vol. 18, no. 8, pp. 2111–2125, 2017. DOI: 10.1109/TITS.2016.2633999.

[34] D. Q. Huang, J. X. Xu, X. Deng, V. Venkataramanan, T. C. T. Huynh. Differential evolution based high-order peak filter design with application to compensation of contact-induced vibration in HDD servo systems. *International Journal of Automation and Computing*, vol. 14, no. 1, pp. 45–56, 2017. DOI: 10.1007/s11633-016-1034-y.

[35] A. R. Jimnez, F. Seco, J. C. Prieto, J. Guevara. Indoor pedestrian navigation using an INS/EKF framework for yaw drift reduction and a foot-mounted IMU. In *Proceedings of the 7th Workshop on Positioning, Navigation and Communication*, IEEE, Dresden, Germany, pp. 135–143, 2010. DOI: 10.1109/WPNC.2010.5649300.

[36] N. Agrawal, A. Kumar, V. Bajaj, G. K. Singh. High order stable infinite impulse response filter design using cuckoo search algorithm. *International Journal of Automation and Computing*, vol. 14, no. 5, pp. 589–602, 2017. DOI:

10.1007/s11633-017-1091-x.

[37] Y. L. Hsu, J. S. Wang, C. W. Chang. A wearable inertial pedestrian navigation system with quaternion-based extended Kalman filter for pedestrian localization. *IEEE Sensors Journal*, vol. 17, no. 10, pp. 3193–3206, 2017. DOI: 10.1109/JSEN.2017.2679138.

[38] Y. S. Shmaliy, S. Y. Zhao, C. K. Ahn. Unbiased finite impluse response filtering: An iterative alternative to Kalman filtering ignoring noise and initial conditions. *IEEE Control Systems Magazine*, vol. 37, no. 5, pp. 70–89, 2017. DOI: 10.1109/MCS.2017.2718830.

[39] S. Y. Zhao, Y. S. Shmaliy, C. K. Ahn, F. Liu. Adaptive-horizon iterative UFIR filtering algorithm with applications. *IEEE Transactions on Industrial Electronics*, vol. 65, no. 8, pp. 6393–6402, 2018. DOI: 10.1109/TIE.2017.2784405.

[40] Y. S. Shmaliy, F. Lehmann, S. Y. Zhao, C. K. Ahn. Comparing robustness of the Kalman, H_{inf}, and UFIR filters. *IEEE Transactions on Signal Processing*, vol. 66, no. 13, pp. 3447–3458, 2018. DOI: 10.1109/TSP.2018.2833811.

[41] S. Y. Zhao, Y. S. Shmaliy, P. Shi, C. K. Ahn. Fusion Kalman/UFIR filter for state estimation with uncertain parameters and noise statistics. *IEEE Transactions on Industrial Electronics*, vol. 64, no. 4, pp. 3075–3083, 2017. DOI: 10.1109/TIE.2016.2636814.

[42] L. L. Bu, Y. Zhang, Y. Xu, X. Y. Chen. Robust tightly-coupled INS/UWB-integrated human localization using UFIR filtering. In *Proceedings of Instrumentation and Measurement Technology Conference*, IEEE, Houston, USA, 2018. DOI: 10.1109/I2MTC.2018.8409558.

[43] Y. Xu, X. Y. Chen, J. Cheng, Q. J. Zhao, Y. M. Wang. Improving tightly-coupled model for indoor pedestrian navigation using foot-mounted IMU and UWB measurements. In *Proceedings of IEEE International Instrumentation and Measurement Technology Conference*, IEEE, Taipei, China, 2016. DOI: 10.1109/I2MTC.2016.7520489.

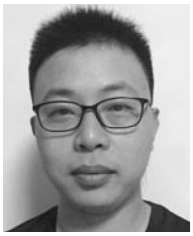

Yuan Xu received the B. Sc. degree in automation from Shandong Polytechnic University, China in 2007, the M. Sc. degree in detection technology and automation device from Shandong Polytechnic University, China in 2010, and the Ph. D. degree in instrument science from Southeast University, China in 2014. He is currently a lecturer of School of Electrical Engineering with the University of Jinan, China. He is a member of IEEE.

His research interests include integrated navigation and robust filtering.

E-mail: xy_abric@126.com (Corresponding author)
ORCID iD: 0000-0002-5966-945X

Tao Shen received the Ph. D. degree in control theory and control engineering at Zhejiang University, China in 2004. Now he is the vice president of School of Electrical Engineering, University of Jinan, China.

His research interests include stability of systems, intelligent control theory and method, robust control and production process control.

E-mail: cse_st@ujn.edu.cn

Xi-Yuan Chen received the B. Sc. degree in mechanical engineering from Lanzhou University of Technology, China in 1990, the M. Sc. degree in mechanical engineering from Hefei University of Technology, China in 1995, and the Ph. D. degree in precision instrument and mechanical engineering from Southeast University, China in 1998. He is currently the professor of School of Instrument Science and Engineering, Southeast university, China. He is a senior member of IEEE.

His research interests include inertial navigation and integrated measurement.

E-mail: chxiyuan@seu.edu.cn

Li-Li Bu received B. Sc. degree in automation from the University of Jinan, China in 2016, and now is a master student in control engineering at the University of Jinan, China.

Her research interest is indoor pedestrian positioning.

E-mail: bu18366105277@163.com

Ning Feng received B. Sc. degree in automation from the University of Jinan, China in 2017, and now is a master student in control engineering at the University of Jinan, China.

His research interest is integrated navigation for indoor robots.

E-mail: fengningjn@foxmail.com